Fundamental Mechanisms Driving the Amorphous to Crystalline Phase Transformation

B. W. Reed, N. D. Browning, M. K. Santala, T. LaGrange, G. H. Gilmer, D. J. Masiel, G. H. Campbell, S. Raoux, T. Topuria, S. Meister, Y. Cui

January 5, 2011

Disclaimer

This document was prepared as an account of work sponsored by an agency of the United States government. Neither the United States government nor Lawrence Livermore National Security, LLC, nor any of their employees makes any warranty, expressed or implied, or assumes any legal liability or responsibility for the accuracy, completeness, or usefulness of any information, apparatus, product, or process disclosed, or represents that its use would not infringe privately owned rights. Reference herein to any specific commercial product, process, or service by trade name, trademark, manufacturer, or otherwise does not necessarily constitute or imply its endorsement, recommendation, or favoring by the United States government or Lawrence Livermore National Security, LLC. The views and opinions of authors expressed herein do not necessarily state or reflect those of the United States government or Lawrence Livermore National Security, LLC, and shall not be used for advertising or product endorsement purposes.

Fundamental Mechanisms Driving the Amorphous to Crystalline Phase Transformation

Tracking Number 08-ERD-032

Te
Ge
Sb
Vacancy

Laser-pulse driven photoelectron cathode

Cathode laser
Nd:YLF
(5w) l = 211nm
10 ns FWHM pulse

e⁻s

Specimen drive laser
Nd:YAG
λ= 1064, 532 or 355nm
12 ns FWHM pulse

Specimen

CCD camera
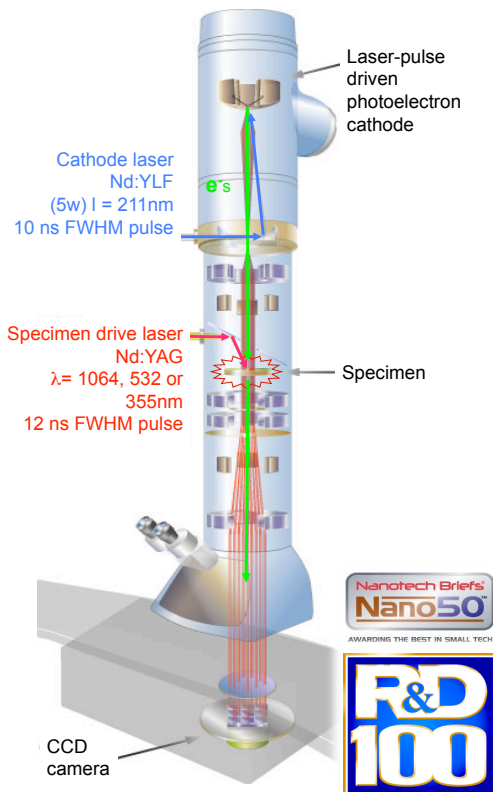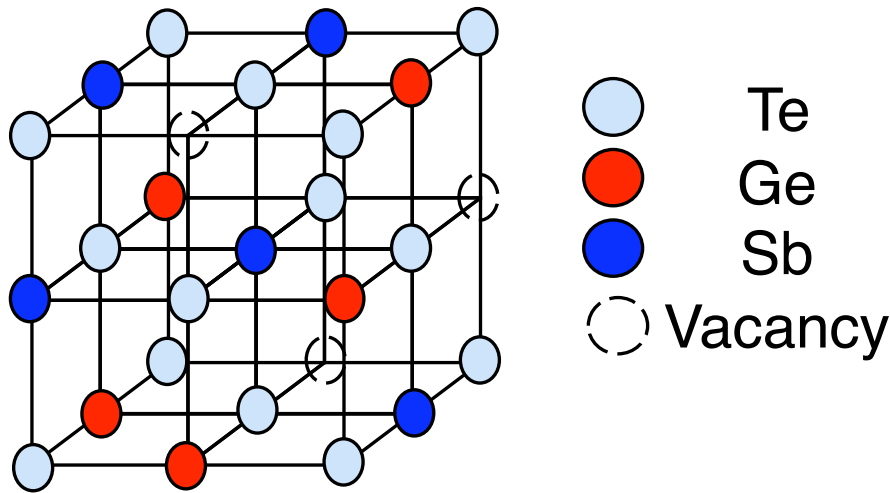
Principal Investigator
N. D. Browning

LLNL Co-Investigators
B. W. Reed
M. K. Santala
T. LaGrange
G. H. Gilmer
D. J. Masiel
G. H. Campbell

Collaborative Co-Investigators
S. Raoux and T. Topuria, IBM
S. Meister and Y. Cui, Stanford University

Introduction

Phase transformations are ubiquitous, fundamental phenomena that lie at the heart of many structural, optical and electronic properties in condensed matter physics and materials science [1]. Many transformations, especially those occurring under extreme conditions such as rapid changes in the thermodynamic state, are controlled by poorly understood processes involving the nucleation and quenching of metastable phases. Typically these processes occur on time and length scales invisible to most experimental techniques (μs and faster, nm and smaller), so our understanding of the dynamics tends to be very limited and indirect, often relying on simulations [2] combined with experimental study of the "time infinity" end state. Experimental techniques that can directly probe phase transformations on their proper time and length scales are therefore key to providing fundamental insights into the whole area of transformation physics and materials science. LLNL possesses a unique dynamic transmission electron microscope (DTEM) capable of taking images and diffraction patterns of laser-driven material processes with resolution measured in nanometers and nanoseconds (Fig. 1) [3]. The DTEM has previously used time-resolved diffraction patterns to quantitatively study phase transformations that are orders of magnitude too fast for conventional *in situ* TEM [4]. More recently the microscope has demonstrated the ability to directly image a reaction front moving at ~13 nm/ns and the nucleation of a new phase behind that front (figure 1) [5].

Fig. 1: The DTEM combines pulsed lasers with a transmission electron microscope to enable direct visualization of fast processes on the scale of nanometers and nanoseconds.
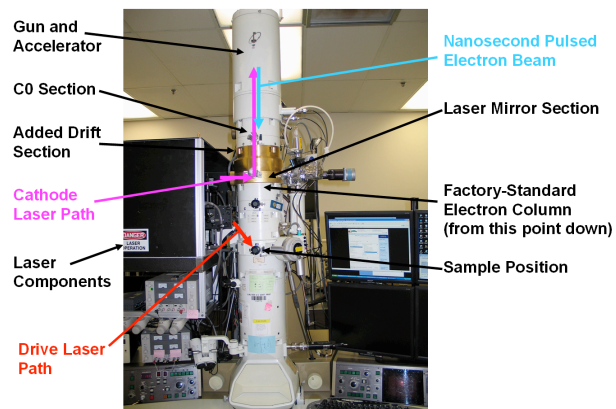
Certain compound semiconductor phase change materials, such as $Ge_2Sb_2Te_5$ (GST), Sb_2Te and GeSb, exhibit a technologically important series of transformations on scales that fall neatly into the performance specifications of the DTEM. If a small portion of such material is heated above its melting point and then rapidly cooled, it quenches into an amorphous state. Heating again with a less intense pulse leads to recrystallization into a vacancy-stabilized metastable rock salt structure [6-10] (Fig. 2). Each transformation takes ~10-100 ns, and the cycle can be driven repeatedly a very large number of times with a nanosecond laser such as the DTEM's sample drive laser. These materials are widely used in optical storage devices such as re-writable CDs and DVDs, and they are also applied in a novel solid state memory technology – phase change memory (PCM). PCM has the potential to produce

nonvolatile memory systems with high speed, extreme density, and very low power requirements [6]. For PCM applications several materials properties are of great importance: the resistivities of both phases, the crystallization temperature, the melting point, the crystallization speed, reversibility (number of phase-transformation cycles without degradation) and stability against crystallization at elevated temperature. For a viable technology, all these properties need to have good scaling behavior, as dimensions of the memory cells will shrink with every generation.
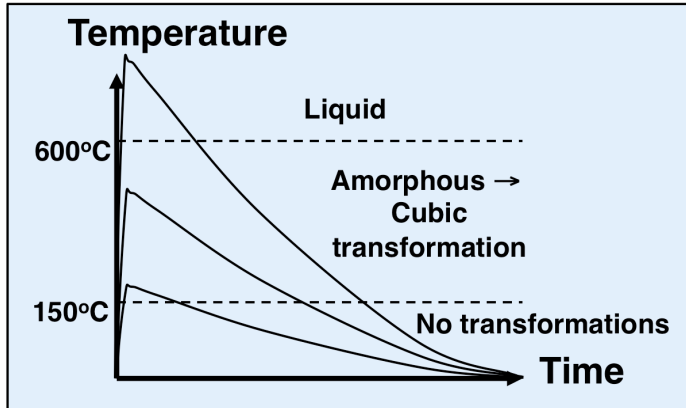
Fig. 2: Heating/cooling curves and associated transformations in $Ge_2Sb_2Te_5$. Cooling time scales range from <100 ns to many μs depending on geometry. To produce the amorphous state, the material must transition between the two temperatures shown faster than the crystalline phase can nucleate.

In this LDRD project, we used the unique single-shot nanosecond *in situ* experimentation capabilities of the DTEM to watch these transformations in GST on the time and length scales most relevant for device applications. Interpretation of the results was performed in conjunction with atomistic and finite-element computations. Samples were provided by collaborators at IBM and Stanford University. We observed, and measured the kinetics of, the amorphous-crystalline and melting-solidification transitions in uniform thin-film samples. Above a certain threshold, the crystal nucleation rate was found to be enormously high (with many nuclei appearing per cubic μm even after nanosecond-scale incubation times), in agreement with atomistic simulation and consistent with an extremely low nucleation barrier. We developed data reduction techniques based on principal component analysis (PCA), revealing the complex, multi-dimensional evolution of the material while suppressing noise and irrelevant information. Using a novel specimen geometry, we also achieved repeated switching between the amorphous and crystalline phases enabling *in situ* study of structural change after phase cycling, which is relevant to device performance. We also observed the coupling between the phase transformations and the evolution of morphology on the nanometer scale, revealing the gradual development of striations in uniform films and preferential melting at sharp edges in laser-heated nanopatterned GST. This nonuniform melting, interpreted through simulation as being a direct result of geometrical laser absorption effects, appears to be responsible for a marked loss in morphological stability even at moderate laser intensities and may be an important factor in the longevity of nanostructured phase change materials in memory applications.

Studies and Results

In the discussion below, we will use term the "forward transformation" to refer to the crystallization of amorphous GST into the vacancy-stabilized rock salt structure, while "reverse transformation" refers to the rapid melt and resolidification of the initially crystalline GST resulting in a frozen-in amorphous state (Fig. 2).

The transformations were studied in detail through a series of conventional and pulsed selected-area diffraction and real-space imaging measurements in the DTEM. Conventional measurements provide convenient exploration of the phase space (e.g. determining the kinds of transformations that can be produced with various laser pulse intensities and pulse counts) and high-quality standard patterns for interpretation of the pulsed experiments. Pulsed measurements provide the crucial element of time resolution, showing us not only what happened but when, and whether there were any intermediate states invisible to conventional long-exposure microscopy.

Three sample geometries were used. The first consisted of uniform thin films of GST deposited in amorphous form onto amorphous SiN_x membrane substrates, often covered with a capping layer such as amorphous AlO_x for the sake of morphological stability during melting and resolidification. Several preparations were used, with typical film thicknesses of ~50 nm for the GST and SiN_x and ~5 nm for the capping layers. These samples were used for studying the nucleation of the crystalline phase, as well as melting and relatively slow resolidification, in the case of uniform heating and cooling over a large area ~50 μm in diameter. The second geometry was identical to the first except that the GST layer was patterned using photolithography to produce disks and crosses on the μm and sub-μm scale. Since the support and capping layers absorb very little of the 1.06 μm and 532 nm light provided by the DTEM's drive laser, almost all of the absorption in this case was in the GST. While this provides faster cooling rates than are possible in the uniform-film geometry, the rates are still not high enough to freeze in the amorphous state, in part because of the extreme nonuniformity of the laser absorption. The third geometry consisted of a thin film of GST deposited onto a long, sharp wedge of Al-coated Si. This geometry was designed to place a large heat sink in close contact with the GST, yielding the ability to lock the material into the amorphous state with sufficiently intense drive laser pulses, while the crystalline state could be recovered through less intense heating.

The experiments fell into a number of general categories, which we will now describe along with data analysis and computational approaches to understanding the results.

<u>Forward transformation and melting/resolidification in a uniform-film geometry.</u> Conventional and pulsed selected-area diffraction revealed the structural transformations in GST in very small volumes of material—typically a region ~10 μm in diameter and ~50 nm thick. The high atomic numbers in the GST allow its diffraction pattern to be clearly visible on top of the signal from the amorphous SiN_x

substrate, even in the amorphous and liquid phases. Long-exposure (conventional) diffraction patterns allowed us to calibrate the laser intensities required for nucleation and growth of the crystalline phase (Fig. 3a-c), while short-exposure patterns revealed the dynamics (Figs. 3-5). A moderate drive intensity produced an enormous number of nanometer-scale crystalline grains (Fig. 3b), producing smooth continuous-ring patterns (indicative of hundreds of grains within the selected area) even from areas as small as 2 μm in diameter. Thus we know that the nucleation density can surpass many hundreds of nuclei per cubic μm. Remarkably, the transformation is already significantly underway by 50 ns and is essentially complete by 300 ns (Fig. 4-5). The transformation to the microcrystalline state through the process of grain coarsening is much slower (Fig. 3c), requiring either multiple drive laser pulses (each of which leaves the sample at elevated temperature for many μs) or a much higher drive laser intensity. In contrast to the nanocrystalline material in which the grain orientations are largely random, the microcrystalline material is significantly textured, eventually reaching a pure [111] fiber texture as expected for a thin film with an fcc Bravais lattice. This is visible in the relative intensities of the Bragg peaks—note the red and green curves on the left-hand side of Fig. 5.

Fig. 3: A series of selected-area diffraction patterns of a supported, uniform film of GST, as described in the text. We see the rapid transition to the nanocrystalline state (a-b), the slower transition to the microcrystalline state (b-c), and the fast melting and resolidification of the microcrystalline state (d-f).
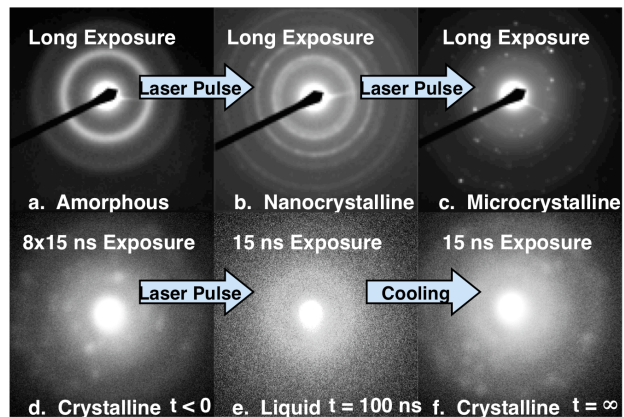
At higher laser intensities, we were able to completely melt the GST in a small region, producing a diffraction pattern entirely lacking Bragg spots and somewhat different from the pattern for as-deposited amorphous GST (Fig. 3e). As the material cools, it solidifies into an ensemble of crystalline orientations distinct from the pre-melting state, as evidenced by the shift in Bragg spots (Fig. 3f). At lower intensities (not shown), the material partially melts and resolidifies into much the same set of grain orientations as it had before the pulse, indicating that the crystalline phase grows into the liquid from any pre-existing grains. The GST would dewet from the substrate rapidly above the threshold for complete melting, such that the experiment could only be repeated a few times before the formerly uniform film looked like water droplets on a clean windshield. At no time did the amorphous diffraction pattern re-emerge in the cooled material, suggesting that the μs-scale cooling rates achievable in the uniform-film geometry simply are not adequate for freezing in the amorphous state of GST, and certainly not without gross morphological change during the long cool-down.

Fig. 4: Rotationally-averaged diffraction patterns showing (above) the amorphous "before" and crystalline "after" states as measured in conventional long-exposure diffraction, and (below) a series of short-pulse measurements showing that the transition between the two states has already begun even at as short a time as 50 ns.
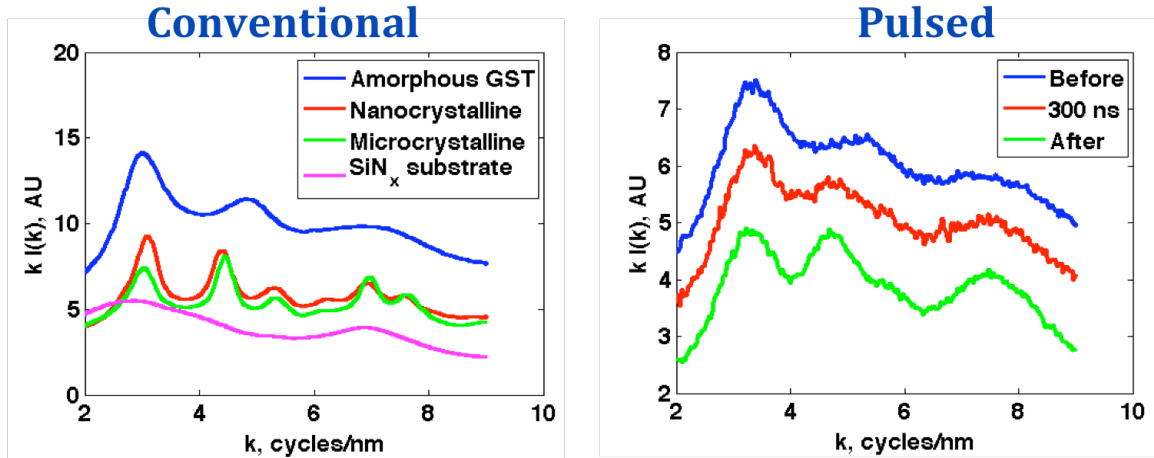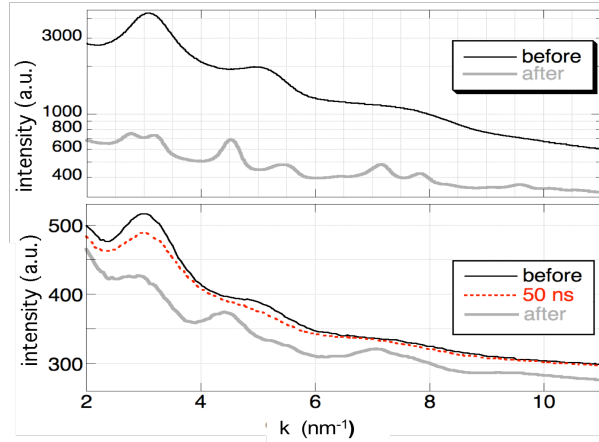
Fig. 5: Rotationally-integrated patterns showing (left) the signatures of various properties including crystallinity, grain size/texturing, and denuding of the substrate, and (right) another pulsed measurement series showing the transition to the nanocrystalline state being almost complete after 300 ns. Beyond this time, the much slower process of grain growth takes over, changing the widths and relative heights of the Bragg peaks.

The extreme nucleation rate is consistent with previous results [11] showing that GST crystallization kinetics are limited by growth and not nucleation. It is also consistent with our own atomistic simulation results, some of which are shown in Fig. 6. This result demonstrates that the time and length scales accessible through atomistic simulation are now overlapping the time and length scales accessible through experiments. We chose to study a closely related binary material SbTe, thus avoiding the difficulties of developing a complicated ternary molecular dynamics potential. Like GST, SbTe is believed to have an extremely low activation barrier for nucleation and to transform in a manner phenomenologically similar to GST.

Time after quench = 5 ns   **Time = 10 ns; CF = 0.62**   **Time = 20 ns; CF = 0.76**
Crystal Fraction = 0.56
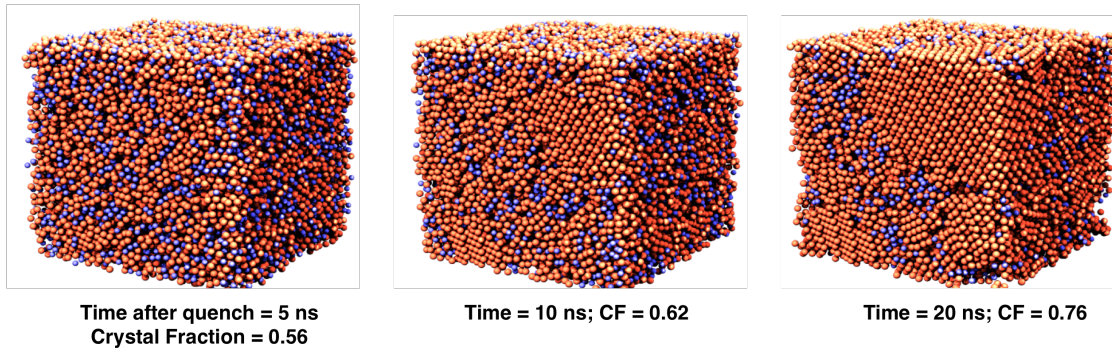
Fig. 6: Example atomistic simulation volume of SbTe (a related material to GST) with 32000 atoms using a hybrid Monte Carlo/molecular dynamics approach designed to achieve thermodynamically correct states on the time scale of many nanoseconds. For purposes of the simulation, the material was quenched from the liquid state to a temperature just below the melting point, and the fraction of material in a crystalline state (CF) was calculated in post-processing. Roughly consistent with the experiments, the majority of the material has structured into nanometer-scale grains even after only 20 ns.

In order to make sense of our large diffraction pattern data sets, comprising hundreds of patterns representing conventional and pulsed measurements of crystalline, amorphous, and liquid GST, we developed a data analysis methodology based on principal component analysis (PCA). PCA is a way of representing the patterns of variance in a large set of vectors by using a small number of eigenvectors (or principal components), each of which accounts for a fraction of the total variance in the entire data. In our case, each rotationally integrated diffraction pattern is taken to be a vector, after being normalized to a mean of zero and a variance of 1. We construct the covariance matrix for the set of all such vectors in one set of measurements (typically ~100) and diagonalize this matrix to produce the principal-component representation. Each diffraction pattern is then represented as a set of coefficients or "scores," one score for each principal component, describing exactly how that pattern differs from the average. The scores are also linearly uncorrelated across the full data set; knowing some of the scores for one diffraction pattern provides very little information on the remaining scores.

The essence of PCA is this: The great majority of the reliable information distinguishing one pattern from another is encoded in just the first few scores. We found that typically almost 95% of the non-noise information in each data set could be represented with just 6 scores per diffraction pattern. Further, the remaining ~5% of the information typically included trivial information about the measurement conditions (e.g. the difference in reciprocal space resolution between pulsed and conventional TEM modes) rather than about anything interesting happening in the sample itself. Thus each pattern could be represented as a set of 6 numbers—a point in a six-dimensional space—instead of as a continuous curve with many points, while filtering out noise and trivial measurement variations. We also performed a related technique called independent component analysis (ICA), which is based on the notion of statistical independence rather than on the weaker but

more mathematically tractable notion of linear uncorrelatedness. The results for ICA were rather similar to the results for PCA, and we elected to use the PCA results for the sake of its simpler mathematics.

In Fig. 7 we represent one of these sets of experiments in exactly such a six-dimensional space. Each diffraction pattern is represented by a sphere. The first three scores (C_1, C_2, and C_3) yield the three-dimensional position of a sphere, while the next three (C_4, C_5, and C_6) determine the red, green, and blue components of the sphere's color. Thus two points that are close to each other in both space and color represent very nearly identical diffraction patterns, apart from noise and mostly trivial measurement variations. The entire data set can now be visualized at a glance. There are several obvious clusters of points in the six-dimensional space, and by comparing with the experimental conditions associated with each cluster, we can identify signposts associated with each. We can even produce a representative diffraction pattern of each, constructed from just the first 6 eigenvectors, with very high signal-to-noise ratios. In effect, these patterns are averaged from the relevant parts of all similar patterns in the entire data set. These are also shown in Fig. 7. Roughly speaking, spheres start out red and become more orange as they transition from amorphous to nanocrystalline, then become yellow-green and increase their C_2 score as they coarsen. The material thickness is largely encoded in C_1, with thick, large-grained material appearing as yellowish spheres with very large C_1 values while the denuded SiN_x substrate appears as cyan spheres with negative C_1 values.
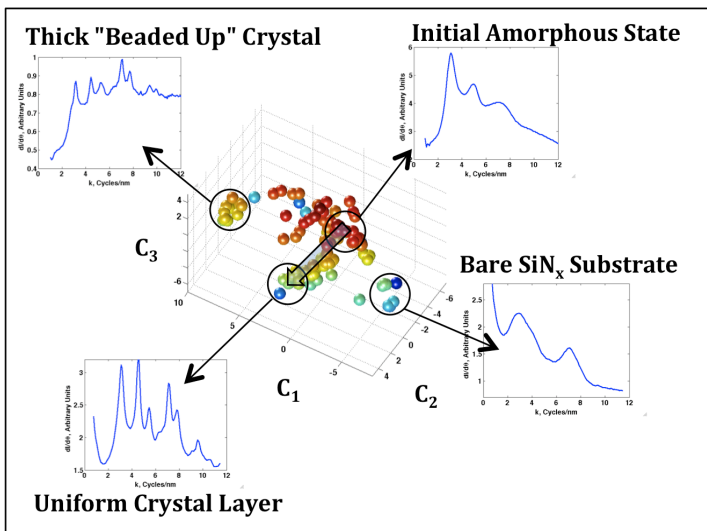
Fig 7. The first 6 components of PCA space shown as colored points in an abstract space. Each sphere is one diffraction measurement. Signposts for "standard" patterns are identified, allowing the data analyst to qualitatively identify multiple parameters of crystallinity, texturing, and morphological change at a glance. Quantitative estimates of phase fractions and sample temperatures can also be generated from the same data.

The pulsed and conventional TEM diffraction measurements are analyzed and plotted as a unit; there is no need to split them out separately. Thus the conventional measurements, with their high signal-to-noise ratios, act as reliable and precise calibration points for interpreting the far noisier pulsed diffraction data. This is a significant advance over simpler analysis methods, and we expect that the PCA approach will become a standard tool for quantitative analysis of DTEM diffraction data.

We also note that a small k-axis rescaling parameter greatly improves the PCA results, significantly reducing the total variance in the data set while apparently eliminating no reliable information about the material transformations. Each diffraction pattern is rescaled horizontally by a constant ratio from ~0.9 to ~1.1. This accounts for two things: (1) Variation in apparent camera length resulting from changes in sample height and TEM alignment and focus, and (2) thermal expansion. Variation (1) mostly corrects for day-to-day and sample-to-sample variability and seems to be quite stable over a time scale of several hours on one sample. Variation (2), which measures the sample temperature, carries important information that is difficult to measure through any other means. DTEM samples, upon being hit with a pulsed laser and allowed to cool, undergo extreme spatiotemporal temperature gradients. The sample temperature at the time of observation is thus difficult to determine precisely. With this axis-rescaling PCA approach, we can produce a temperature estimate with an absolute-temperature precision of perhaps 15% from a 15-nanosecond exposure. The results are suggestive enough that a systematic study is warranted. This, too, is likely to become a standard element in the DTEM-data-analysis tool kit.

<u>Melting and recrystallization, and concomitant beading-up, in a uniform-film geometry.</u> As briefly discussed above, besides the simple crystallization process already described, the material also undergoes morphological change at higher temperatures. While we do observe striations building up slowly over a large number of moderate-intensity drive pulses (below the melting threshold for the sample material; see the left-hand image in Fig. 8), the extreme case of this is when the material actually melts. The heat of fusion of GST is quite high while its thermal conductivity is quite low. Thus, unless a large heat sink is extremely close by, any liquid sample material will remain liquid for multiple μs. We find that this is long enough for surface tension to cause the GST to bead up into droplets which then slowly solidify into the crystalline phase. We have even caught this process in the act, both in real-space and in reciprocal space (Figs. 3, 8). While some thickness variations have developed by 200 ns, the great majority of the morphology change occurs much later. The liquid GST also produces a diffraction pattern that, in the PCA representation, is rather different from that of amorphous GST.

The striations may arise from an unfortunate instability in the laser-driven transformation, based on the fact that the crystalline GST absorbs much more light than does the amorphous GST. This fact is responsible for the high optical-readout contrast between 0 and 1 states in rewritable DVD's. The problem is that some of the material, either because of nonuniformity in the film or pure chance governed by the statistics of nucleation, will become crystalline before the rest. On subsequent laser pulses—or even during the same laser pulse—these early-transforming regions should absorb more light, causing nearby material to crystallize faster as well. Since the DTEM drive laser pulse is only 12 ns long, and the GST's thermal conductivity is relatively low, this produces a characteristic size scale for the hot spots on the order of tens of nanometers, consistent with the images in Fig. 8. While we initially thought that these features were just the initial phases of liquid beading (consistent with other DTEM measurements on a different

material system [5]), on closer inspection of the data we found that they would gradually build up over many pulses even below the threshold for partial melting of the film. This results in the subtle contrast variations in the left-hand image of Fig. 8 (the as-deposited amorphous film showing no such contrast, looking like a uniform field of gray at this magnification). In the middle image, the GST near the middle of the field of view is actually entirely liquid at this time and is starting to bead up. It is quite possible that these striations are the direct descendants of the structures weakly appearing in the left-hand image, which were created entirely in the solid state. Further experiments focused directly on this phenomenon should be able to clarify this question directly. The current results show the relevance of DTEM for studying the coupling between light absorption, transformations, and morphology changes that are so important for the reliable use of this class of materials in memory applications.
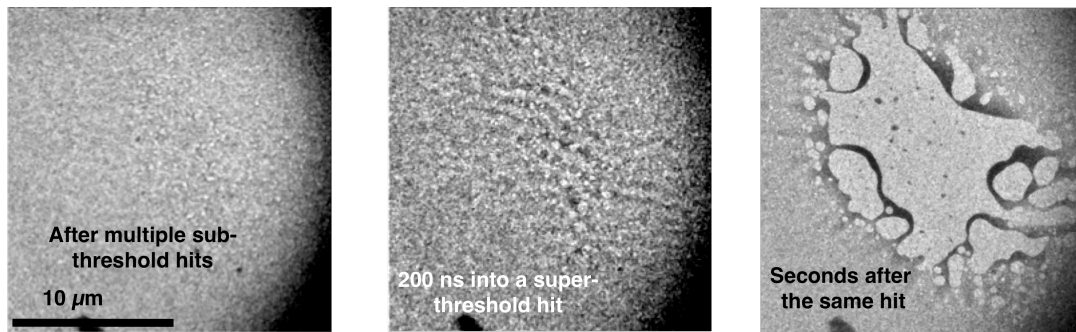
Fig. 8: A pulsed before-during-after sequence of complete melting of a region of nanocrystalline GST that had previously been hit by a large number of low-intensity laser pulses sufficient to cause nucleation but little growth of the crystalline grains.

Forward and reverse transformations in a novel coated-wedge geometry. Rapid cooling in a TEM sample is rather difficult to achieve, for simple reasons of geometry: TEM samples need to be thin enough for electron transparency over a region large enough for meaningful measurement of microstructure and crystallinity. Thus the material of interest is usually very far from any substantial heat sinks. By the laws of heat diffusion, cooling times in TEM samples are almost always on the scale of μs or ms. Resolidification of GST into the amorphous phase requires cooling rates on the order of 10^9 K/s, much faster than are achievable in a standard DTEM experiment. This is why the results described thus far only show the forward transformation and not the reverse transformation.
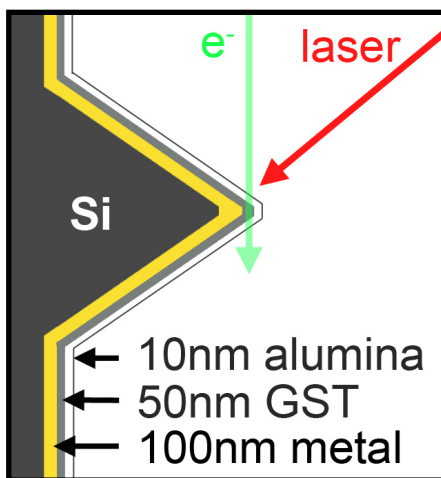
Fig. 9: The wedge geometry enabling extreme cooling rates in DTEM experiments

We overcame this problem by developing the sample geometry shown in Fig. 9, in which a sharp wedge of Si is coated first with a highly

conductive metal and then with the GST, followed by a capping layer of AlO$_X$ for stability during melting and resolidification. The electron beam can pass through a small, thin region of GST exposed at the end of the wedge. The metal and silicon act as large heat sinks directly in contact with the GST, allowing the cooling rate to reach the extreme levels needed for the reverse transformation. With this geometry, we successfully transformed the material back and forth between the crystalline and amorphous phases multiple times, as measured in conventional diffraction (Fig. 10).
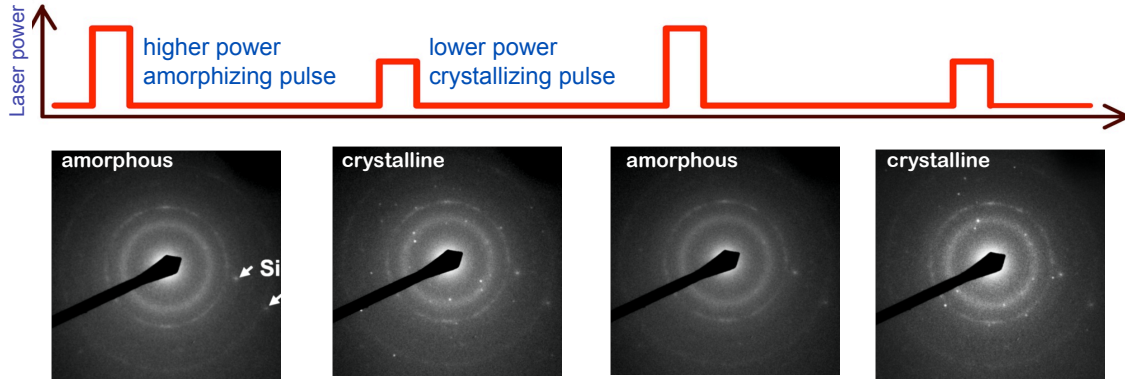
Fig. 10: Schematic drive laser pulse intensity sequence to produce a sequence of repeated crystallization/amorphization cycles, as evidenced in the diffraction patterns. Bragg spots in the amorphous patterns are actually from the crystalline Si substrate.

Melting, resolidification, and grain coarsening in a nanopatterned geometry. In our efforts to reduce the volume of heated material and thus increase the cooling rate towards the level required for amorphization, we studied a set of samples similar to the uniform-film samples except for an extra photolithography step, producing arrays of disks and crosses with features on the μm and sub-μm scales (Fig. 11). The GST was nanocrystalline in the as-received material, thus these samples were appropriate for studying the melting and resolidification processes.
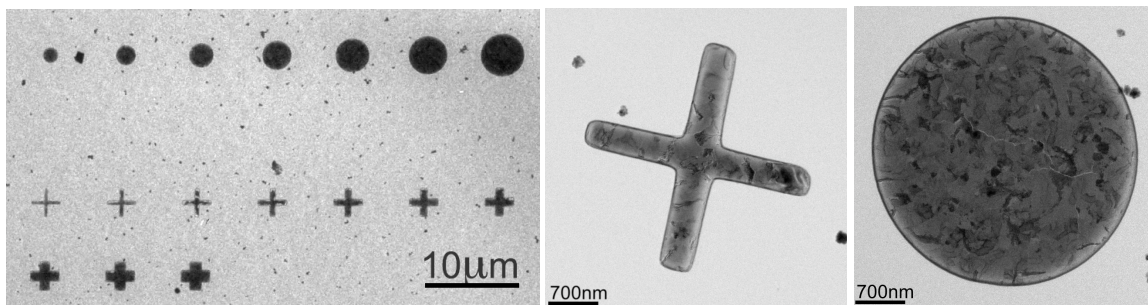
Fig. 11: Conventional TEM images of the nanopatterned GST samples, including disks and crosses with a variety of sizes.

We observed that it was not possible to uniformly melt the samples with the 12 ns FWHM DTEM sample drive laser pulse. Instead, certain regions around the edge of a disk would consistently melt and start to bead up, even at laser fluences so low that the material in the middle of the disk showed little or no grain coarsening. More often than not, the melting in different disks initiated at roughly the same regions relative to the incident direction of the drive laser, though some individual disks with obvious pre-existing microstructure (e.g. cracks and voids) provided exceptions to this behavior.

There are two likely physical effects that could contribute to the observed geometrical variation in melting. The first is the Gibbs-Thomson effect, whereby the thermodynamic properties of regions of extremely high surface curvature differ from those of the bulk. In our case, we may expect a reduction of the melting point at the sharp edges of the nanostructured GST. While this may be a contributing factor to the observed effects, it would not account for either the apparent extreme difference in temperatures or the relatively consistent spatial positioning of the enhanced melting. The second effect, geometrical laser absorption variation, could account for both. Maxwell's equations predict that a light wave that strikes a material with features smaller than the light's wavelength will typically result in greatly enhanced electromagnetic field intensities, particularly at sharply convex features such as edges and points. This means that the absorption of the light will also be concentrated at such features. Because the GST has a low thermal conductivity, this means that, during the 12 ns drive pulse, the material within ~50 nm of sharp corners and edges may get considerably hotter than the rest of the material. Some tens of nanoseconds later (proportional to the square of the nanostructure radius), the temperature will be essentially equilibrated. Unfortunately, by this time the damage will have already occurred, in the form of rapid beading-up of the liquid phase under the influence of surface tension. This behavior is consistent with DTEM observations (Fig. 12).

Before   During, 4ns delay   After
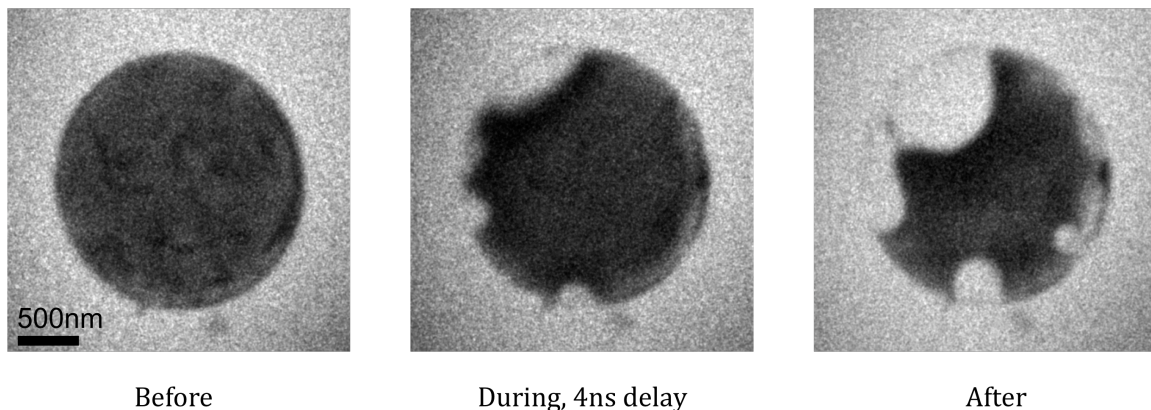
Fig. 12: DTEM image series of a GST disk struck with a laser pulse of sufficient intensity to melt much of the disk. The DTEM's drive laser pulse is 12 ns in duration, while the exposure time is 15 ns. Thus the middle image, taken during the melting process with a 4 ns delay between drive and exposure pulses, involves a very substantial overlap of the two temporal pulses; it is truly taken *during* the actual laser absorption. It is clear that most of the melting initiates at or near the edges, and that a substantial fraction of the change in shape of the disk happens extremely quickly--near the limit of time resolution even of the DTEM.

1.06 μm P-polarized

532 nm S-polarized

532 nm P-polarized
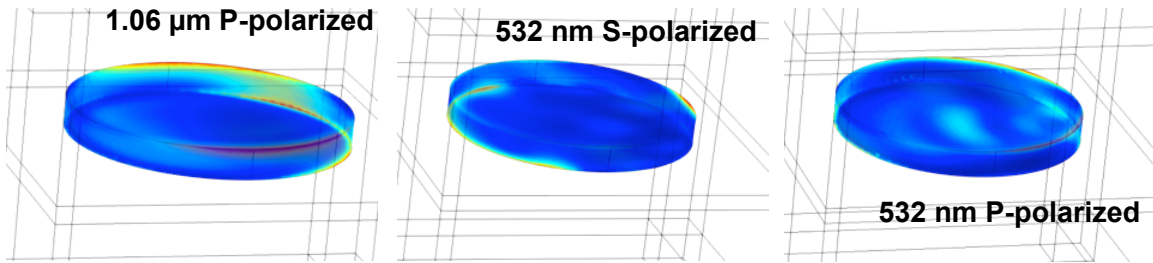
Fig. 13: **Representative COMSOL simulations, showing the three-dimensional patterns of absorption in a GST disk lying on a SiN$_x$ substrate, using (left and center) the actual laser drive conditions in the DTEM, and (right) an alternative drive condition that could be achieved with a slight change in the DTEM's optical configuration, illustrating the distinct effects of wavelength and polarization on the absorption pattern. The absorption is plotted volumetrically using semitransparent coloring to give a sense of the three-dimensional pattern. The laser is incident from the upper left, 42° from normal. Edges of parts of the SiN$_x$ substrate and perfectly matched layers are also shown.**

In order to understand this effect, we embarked on a series of finite-element simulations of laser absorption in the three-dimensional DTEM geometry using the commercial simulation package COMSOL. The calculations were done in a time-harmonic scattered-wave formalism, with the unperturbed field defined as a plane wave incident on the sample from an angle of 42° and either a 1.06 μm wavelength (P-polarized) or a 532 nm wavelength (S-polarized), consistent with the actual drive geometry in the DTEM. COMSOL then calculated, given the geometry and complex dielectric functions of the GST and SiN$_x$, the scattered electromagnetic field. The simulation volume was bounded by perfectly matched layers and scattering boundary conditions, in effect enforcing a boundary condition that no waves are inbound from infinity except for the already-defined incident plane wave. COMSOL then calculated the dielectric losses directly from the electric field amplitudes and the complex dielectric functions. These are plotted in Fig. 13. Note the sharp peaks in absorption at various "corners" of the disks. While the maximum values of these absorption peaks are numerical artifacts caused by the artificially sharp edges of the disks, the positions and spatial extents of the peaks are physically meaningful. The positions depend significantly on laser wavelength and polarization as well as the size of the disk (Fig. 14).
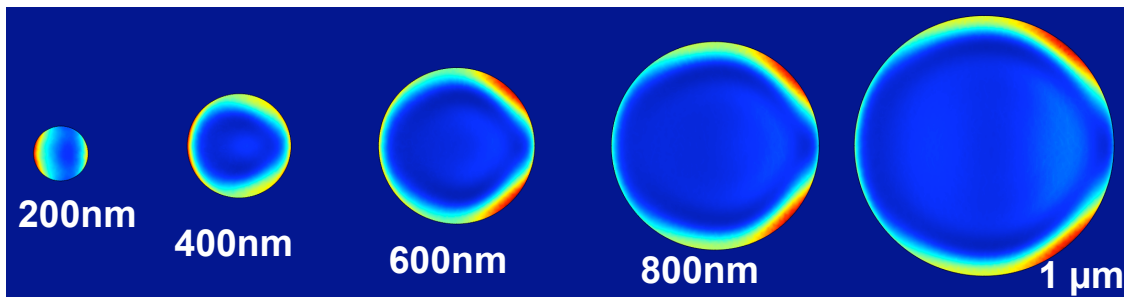
Fig. 14: COMSOL simulations showing the absorption patterns in the midplanes of various-sized GST disks under 1.06 μm P-polarized light incident from the left, 42° from normal.

Conclusions

Our study of the transformation properties of GST combined diverse approaches (conventional and dynamic TEM, principal component analysis, atomistic simulation, and finite-element simulation) to explore the multifaceted complexities of the transformations. Besides obtaining measurements of the nucleation, growth, and coarsening of the crystalline phase and demonstrating repeatable switching between the two metastable phases, we also discovered connections among the transformations, laser absorption, and morphological evolution. These processes are relevant to the long-term stability of these materials under repeated transformation, a key issue in the eventual large-scale development of memory applications of phase change materials. They are also scientifically interesting in their own right, the development of order from disorder on fast an ultrafast time scales being a very broad subject of strong current interest.

The project also developed techniques, including novel sample geometries, data analysis algorithms, and the coupling of simulation and experiment, that are broadly applicable far beyond this class of materials. With these techniques added to our repertoire, the DTEM is now capable of performing experiments with cooling rates perhaps as high as 10^9 K/s, of extracting multiple independent pieces of information (about crystallinity, texture, morphology, phase, etc.) from diffraction data, and of measuring the approximate temperature in a very small volume of material with only a 15 ns exposure time. We are also able to perform experiments at spatiotemporal scales that can now be reached with atomistic simulation, bridging a gap that has limited our scientific understanding of material transformations for a great many years.

References

[1]   G. Kostorz, ed., *Phase Transformations in Materials*, Weinheim, Germany: Wiley-VCH (2001).

[2]   H. Hsieh and S. Yip, "Atomistic Simulation of Defect-Induced Amorphization of Binary Lattices," *Phys. Rev. B* **39**, 7476-7491 (1989).

[3]   W. E. King, G. H. Campbell, A. Frank, B. Reed, J. F. Schmerge, B. J. Siwick, B. C. Stuart, P. M. Weber, "Ultrafast electron microscopy in materials science, biology, and chemistry", *Journal of Applied Physics* **97**, 111101 (2005)

[4]   Thomas B. LaGrange, Michael Armstrong, Ken Boyden, Curtis Brown, Nigel D. Browning, Geoffrey H. Campbell, Jeffrey D. Colvin, Bill DeHope, Alan M. Frank, David J. Gibson, Fred Hartemann, Judy S. Kim, Wayne E. King, Ben J. Pyke, Bryan W. Reed, Richard M. Shuttlesworth, Brent C. Stuart, Ben R. Torralva,

"Single Shot Dynamic Transmission Electron Microscopy for Materials Science", *Applied Physics Letters* **89**, 044105 (2006)

[5]   J.S. Kim, T. LaGrange, B.W. Reed, M.L. Taheri, M.R. Armstrong, W.E. King, N.D. Browning, G.H. Campbell, "Imaging of transient structures using nanosecond in situ TEM," *Science* **321**,1472-1475 (2008).

[6]   M. Wuttig, D. Lusebrink, D. Wamwangi, W. Welnic, M. Gillesen, R. Dronskowski, "The role of vacnacies and local distortions in the design of new phase change materials", *Nature Materials* **6**, 122-128 (2007).

[7]   Z. Sun, J. Zhou, R. Ahuja, "Unique melting behavior in phase-change materials for rewritable data storage", *Physical Review Letters* **98**, 055505 (2007).

[8]   H. F. Hamann, M. O'Boyle, Y. C. Martin, M. Rooks, H. K. Wickramasinghe, "Ultra high density phase change storage and memory", *Nature Materials* **5**, 383-387 (2006).

[9]   M. J. Lankhorst, B. W. S. M. M. Ketelaars, R. A. M. Wolters, "Low cost and nanoscale non-volatile memory concept for future silicon chips", *Nature Materials* **4**, 347-352 (2005)

[10]   M. Wuttig, "Towards a universal memory", *Nature Materials* **4**, 265-266 (2005).

[11]   S. Raoux, "Phase Change Materials," *Annual Review of Materials Research* **39**, 25-48 (2009).